

# Microscopic processes during ultra-fast laser generation of Frenkel defects in diamond

Benjamin Griffiths<sup>1,2</sup>, Andrew Kirkpatrick<sup>1,2</sup>, Shannon S. Nicley<sup>1,3</sup>, Rajesh L. Patel<sup>4</sup>, Joanna M. Zajac<sup>1</sup>, Gavin W. Morley<sup>4</sup>, Martin J. Booth<sup>2</sup>, Patrick S. Salter<sup>2</sup>, Jason M. Smith<sup>1</sup>

<sup>1</sup>*Department of Materials, University of Oxford,  
Oxford, OX1 3PH, United Kingdom*

<sup>2</sup>*Department of Engineering Sciences,  
University of Oxford, Oxford,  
OX1 3PJ, United Kingdom*

<sup>3</sup>*Department of Electrical and Computer Engineering,  
Michigan State University,  
East Lansing, MI 48824, United States*

<sup>4</sup>*Department of Physics, University of Warwick,  
Coventry, CV4 7AL, United Kingdom  
benjamin.griffiths@materials.ox.ac.uk*

(Dated: November 5, 2021)

Engineering single atomic defects into wide bandgap materials has become an attractive field in recent years due to emerging applications such as solid-state quantum bits and sensors. The simplest atomic-scale defect is the lattice vacancy which is often a constituent part of more complex defects such as the nitrogen-vacancy (NV) centre in diamond, therefore an understanding of the formation mechanisms and precision engineering of vacancies is desirable. We present a theoretical and experimental study into the ultra-fast laser generation of vacancy-interstitial pairs (Frenkel defects) in diamond. In a range of other materials, Frenkel defect formation has previously been linked to the recombination of laser generated excitonic states, however the mechanism in diamond is currently unknown and to date no quantitative agreement has been found between experiment and theory. Here, we find that a model for Frenkel defect generation via the recombination of a bound biexciton as the electron plasma cools provides good agreement with experimental data. The process is described by a set of coupled rate equations of the pulsed laser interaction with the material and of the non-equilibrium dynamics of charge carriers during and in the wake of the pulse.

## I. INTRODUCTION

Point defects in crystalline semiconductors and insulators are leading candidates for solid state qubits in quantum technologies [1] [2] [3], the atomic-like energy structure of levels deep within the band gap providing long-lived coherent states [4]. color centres are a class of point defects that display strong optical transitions, which can allow qubit initialisation and readout, and coherent coupling to an optical network [5] [6]. The controlled generation and manipulation of such defects is therefore of great interest. Many color centres take the form X-vacancy, where X is a dopant atom, therefore understanding processes by which vacancies can be generated on-demand is paramount to the development of these technologies. Traditional engineering techniques such as ion implantation [7] and electron irradiation [8] are successful at producing clusters of vacancies, however, often have limited control over the spatial distribution, particularly in the axial direction. This converts into a stochastic yield of color centres with moderate positional accuracy following an annealing step. Direct laser writing with single ultra-fast pulses has recently been shown as a promising way to excite isolated Frenkel defects (bound vacancy-interstitial pairs) in diamond at desired locations, such that subsequent annealing can produce high quality nitrogen-vacancy centres [9][10][11][12]. Similar studies in silicon carbide and gallium nitride reveal that laser writing has the ability to produce a host of different color centres in

wide-bandgap materials [13][14]. Evidence of a lower intensity regime has recently emerged through multi-pulse processing, in which the laser pulse delivers sufficient energy to mobilise the diffusion of vacancies without further Frenkel defect generation or graphitization [15] [16] [17]. These observations open the question of the degree to which point defects can be engineered using ultra-fast laser techniques, and motivate further study.

The physics of ultra-fast optical pulses interacting with diamond has been studied extensively, however most work has focused on higher energy regimes in which dielectric breakdown occurs and the diamond is graphitised [18] [19] [20]. The breakdown process generates carrier densities of a significant proportion of the atomic density, causing a significant shift in the potential energy surface such that a non-thermal melting occurs through a Coulomb explosion on timescales of  $\sim 10$ -100 fs [21] [22]. Re-solidification of this material leads to the formation of  $sp^2$  carbon and voids frozen into the crystal. In addition, longer duration high energy pulses allow for collisions of high energy carriers with lattice ions, which facilitates a thermal melting followed by re-solidification as graphitic material [23]. Surface processing in this regime leads to ablation [24].

At the lower intensity regimes encountered in [9], very different dynamics are expected. The laser pulse generates non-equilibrium charge carriers through a combination of multi-photon absorption, Zener breakdown and avalanche processes, the relative strengths of which are

highly non-linear with respect to the focal intensity [25] [26] [27] [28]. Following the pulse, carriers thermalise rapidly through carrier-carrier scattering to a temperature much higher than the lattice [29]. Scattering with optical and acoustic phonons follows on tens of picosecond timescales such that the excess energy is dissipated into the lattice and the two approach a quasi-equilibrium temperature which decays away through thermal diffusion over several microseconds [30] [31] [32]. The non-equilibrium nature of this system allows for some unusual states of matter including dense excitonic states and at a low enough temperature, condensation into an electron-hole liquid [29]. Such states are long lasting and eventually decay through recombination processes.

In these lower energy regimes, the process of defect generation in diamond has yet to be identified. The localisation of energy from carriers to a single atomic site has been predicted via the self trapping of valence biexcitons, which apply a deformation potential of 1.7 eV to a single atomic site and can lead to the breaking of a carbon-carbon bond [33]. However no clear mechanism for Frenkel defect creation has yet been identified.

Density functional theory calculations reveal a formation energy of 7.14 eV for the neutral vacancy in diamond [34], and that an additional energy barrier of at least 0.6 eV exists between the perfect lattice and the Frenkel defect [35], suggesting that about 8 eV is required to be delivered to a single carbon atom for a Frenkel defect to be created.

The high degree of non-linearity of defect creation with laser pulse energy is a striking feature. To date this non-linearity has been associated solely with the initial photoionisation process and the subsequent energy relaxation leading to defect creation has been assumed to be linear [36] [37]. In the high energy regime, where lattice damage and breakdown is generally proportional to the total carrier density, these models are able to explain experimental data, but in the lower energy regime lattice damage is not proportional to electron density such that more complex interactions become important. We note that others have created models of some of these interactions, often focusing upon the conduction band electron dynamics, however these models are generally simplified so that the equations can be solved analytically such as ignoring the spatial dependence of carriers and energy transfer to the lattice [30] [38]. Furthermore many consider the multi-photon processes as a simple power-law relationship with regards to the focal intensity, not considering the band structure or non-linear propagation of the light through the material. Lagomarsino et al showed that degeneracy between valance bands leads to a non-perturbative enhancement of photoionisation leading to higher non-linearities than would be expected in the generation of free carriers [37]. We find that spatial dependence is key as the high electron densities generated lead to metallic behaviour such that non-linear focusing effects and beam attenuation become important to consider.

Here we seek to develop a quantitative understanding of Frenkel defect generation in diamond by comparing the results of a coupled rate equation model with experiments performed using laser processing. We show that a model in which defect generation occurs via the non-radiative recombination of self-trapped biexcitons combined with thermal excitation over a potential barrier of about 0.5 eV predicts trends that are in good agreement with experiment. Developing understanding of these interactions is key to optimising the processing for the development of quantum technologies.

## II. EXPERIMENTS

The key metric used in this paper is the number of Frenkel defects generated by a single laser pulse focused into a diamond sample. Vacancies with a neutral charge state in diamond fluoresce under green illumination at a wavelength of 740 nm known as GR1 fluorescence [39]. The intensity of this fluorescence under a given set of excitation conditions therefore provides a measure of the number of vacancies present which can be compared with theoretical predictions. The GR1 peak broadens as the lattice becomes less periodic, eventually broadening into a B-band peak indicative of significant dislocations and other damage such as graphitisation.

The diamond sample used in this study is a type 1b single-crystal supplied by Element Six with 2 parts per billion (ppb) nitrogen concentration. Vacancies were generated using single 250 fs pulses from a 790 nm, Ti:Sapphire laser (Spectra Physics Solstice) amplified to pulse energies of 10-20 nJ using a chirped pulse amplifier (CPA) and focused into the diamond at a depth of 20  $\mu\text{m}$  using an oil immersion objective lens (Olympus PlanApo, NA = 1.4). The optical path can be seen in FIG. S1 of the supplementary information. Arrays of sites were processed in which the pulse energy was varied by rotating a half-wave-plate before a polariser and measured at the back focal plane of the objective lens. The beam was reflected off a liquid crystal phase-only spatial light modulator (SLM), (Hamamatsu X10468-02), to adjust for aberrations in focusing and thereby minimise the focal volume of the pulse [18]. The magnitude of the aberrations was minimised through a sensorless adaptive optics regime whereby SLM and laser parameters were altered and optimised through minimisation of the pulse energy required to form graphite from a single pulse and measurement of the contrast of graphitic material formed via an in-situ transmission microscope [18]. Movement between sites in an array was achieved by sample translation on a precision stage (Aerotech air-bearing XYZ) to ensure that the focusing condition remained fixed. Each row of the laser written arrays had 10 sites at 2  $\mu\text{m}$  spacing of the same pulse energy to allow averaging and the range of pulse energies was chosen with a maximum of significant graphitization and a minimum where two thousand pulses produced no visible damage.

Where control of the numerical aperture was required this was achieved by using a blazed grating on the SLM to control the fill factor of the lens. This technique allowed the NA to be varied between 0.95 and 1.4 without changing the objective lens. The laser pulse duration was varied between 120 fs and 1 ps by tuning the compression of the pulse as it passes through the CPA and measured prior to the objective lens via sampling of many pulses by an APE pulse check auto-correlator.

Photoluminescence measurements were carried out with an excitation wavelength of 532 nm at a continuous-wave power of 1.1 mW and fluorescence was collected between 590 nm and 900 nm in a home-built confocal microscope. To determine the fluorescence intensity at a given laser power, 2D Gaussian peaks were fitted to the confocal images of laser written sites giving a value for the brightness from the integrated intensity. The background fluorescence was measured 1  $\mu\text{m}$  from the laser written points which was then subtracted from the intensity value such that the measured intensity value came solely from the laser process. The recorded fluorescence intensity was determined by averaging the measured values from ten sites.

FIG. 1a shows an example of a fluorescence image of an array of laser written sites. Spectral analysis (FIG. 1b) and wide-field transmission imaging reveal that up to 18 nJ the fluorescence is dominated by the GR1 peak at 740 nm, whereas at higher pulse energies a significant B-band peak is observed showing the onset of graphitization. The spectrally integrated fluorescence intensity as a function of write-pulse energy is shown in blue on a logarithmic plot in FIG. 1c. The intensity increases by a factor of 50 between 16 and 18 nJ but then quickly saturates and is approximately linear at pulse energies above 20 nJ. The effect of laser writing on dielectric materials is often described in terms of the level of non-linearity defined as a power-law relationship. A red guide-line showing a power of 33 is marked onto the figure. Overlaid in black is the best fit simulated data from numerically solving the partial differential equation (PDE) model developed in the following section.

### III. RATE EQUATION MODEL

We model the dynamics of the laser pulse interaction with the diamond using a set of coupled non-linear differential equations and solve numerically using finite difference methods describing the evolution of the system from the onset of the pulse to 100 ps after the pulse passes through the focus. This allows sufficient time for all defect generation to occur, although the lattice temperature remains elevated and the heat generated takes a further nanosecond to dissipate. The rate equations are applied over the two spatial coordinates corresponding to the cylindrically symmetric focal spot, covering an axial range of 3  $\mu\text{m}$  about the focal plane and a radial distance of 200 nm, which was found to be large enough that edge

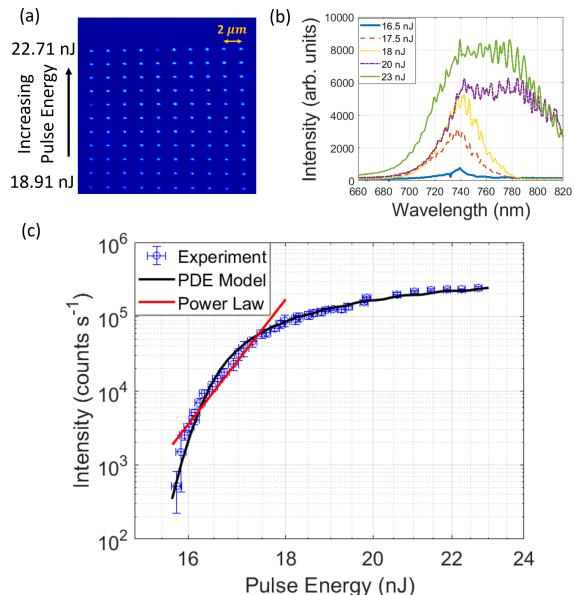


FIG. 1. a. A confocal image of the highest energy sites in the array. b. Spectral composition of laser written sites, fluorescence is centred at a peak at 740 nm corresponding to lattice vacancies which broadens and shifts to longer wavelengths for higher pulse energies indicating further damage and graphitization. c. The average fluorescence intensity measured from single pulses against pulse energy (blue) overlaid with simulated data (black). Shown in red is a guide-line showing a power law of order 33.

effects are negligible. A time-step of 0.1 fs was chosen, a pixel size of 17 nm in radius and 38 nm in depth with an intraband energy resolution of 0.02 eV allowing for a reasonably fine mesh of the region of interest.

We used eight rate equations to model the evolution of the following parameters: (1) optical intensity, (2 and 3) electron and hole concentrations, (4) exciton concentration, (5 and 6) free and self-trapped biexciton concentration, (7) lattice temperature, and (8) Frenkel defect concentration. Carrier concentrations are expressed as distributions over energy up to a maximum of 25 eV. Each rate equation takes the form of a Boltzmann equation [40], modeling the change to the distribution as a sum of all processes that act upon that distribution in phase space. Full details are given in the supplementary information - here we describe the key features.

The optical intensity and electric field as functions of position and time are calculated based on the focal intensity distribution of the focused laser pulse as it propagates through the material, accounting for absorption of photons by electrons within the material and the changes to how the pulse propagates due to the generated electron plasma including self-focusing and filamentation [32] [41]. For the input laser pulse we assume a top-hat intensity distribution with a perfectly aberration-corrected phase distribution at the back focal plane of the objec-

Parameter	value	ref.
Electron-electron scattering	Eq. S4	[44]
Electron-phonon scattering	Eq. S7	[45]
Electron-phonon-photon scattering	Eq. S11	[26]
Radiative electron-hole recombination	2.3 $\mu$ s	[47]
Radiative exciton recombination	350 ns	[48]
Radiative biexciton recombination	7.3 ns	[49]
Radiative self-trapped biexciton recombination	7 ns	[33]
Optical phonon energy	0.15 eV	[46]
Acoustic phonon energy	0.08 eV	[46]
Exciton binding energy	80 meV	[50]
Biexciton binding energy	12 meV	[51]
Biexciton self-trap deformation potential	1.74 eV	[33]
Lattice relaxation energy	4.85 eV	[33]

Table I: Interaction parameters and sources

tive lens and use standard Fourier optics to construct the 3D distribution of the laser intensity profile [42][43]. The temporal evolution is modelled as a Gaussian envelope to the sinusoid at the laser frequency.

The rate equations for free carriers include all relevant generation, recombination, scattering processes and exciton formation (see supplementary information). Generation rates were calculated using the band structure of diamond obtained using density functional theory and numerical integrals were evaluated using the Euler finite difference method. For the interaction rates we use the collision time approximation, drawing values for average interaction times from previous works (table I). This approach allows carrier scattering rates to be evaluated as explicit functions of carrier energy, but averaged over momentum space. This is a reasonable approximation since carrier scattering homogenises the momentum distribution across the Brillouin zone after a few scattering events.

The lattice temperature rate equation has two terms corresponding to lattice heating through carrier-phonon scattering and heat diffusion. We define a graphitization threshold when the carrier density reaches 9% of the atomic density [52] [53] or as when the lattice exceeds the melting temperature (4300 K). An electron temperature was calculated through least squares fitting of an exponential function to the electron distribution.

The rate of formation of excitons was calculated using the local concentration of electron-hole pairs with kinetic energy less than the excitonic binding energy [32] [54], which in diamond is  $\mathcal{E}_X = 80$  meV [50]. The interaction timescale depends upon the Debye length of carriers, which in turn is dependent on values such as the electron temperature and concentration. This timescale is of the same order as the carrier-carrier scattering as both take place through the screened Coulomb interaction so we utilise the same empirical parameter for both processes. Exciton-carrier scattering, exciton-phonon scattering, and recombination processes are also included. Finally the formation and dissociation of biexcitons contributes to the exciton population.

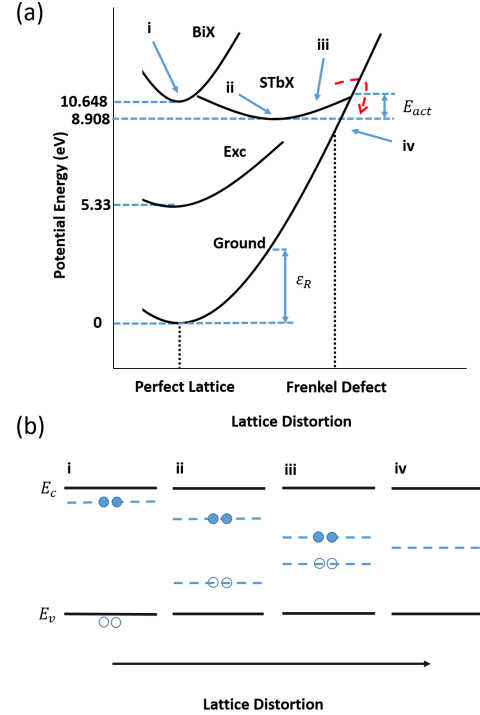


FIG. 2. a. Schematic of the adiabatic potential energy curves of the ground state, free biexciton state (BiX), free exciton state (Exc), and the self-trapped biexciton state (STbX) against lattice distortion. The red dashed line shows possible non-radiative decay processes of the STbX's and the blue dashed lines indicate the activation energy  $E_{act}$  and relaxation energy,  $\epsilon_R$  of the ground state. b. A schematic of the proposed band structure during the non-radiative recombination of the self-trapped biexciton. The bonding, anti-bonding states in the band-gap approach each other as the lattice is further deformed allowing non-radiative recombination.

In a similar manner to exciton formation, the rate of biexcitons formation is calculated from the concentration of pairs of excitons with kinetic energy lower than the biexcitonic binding energy of  $\mathcal{E}_{bX} = 12$  meV [51]. As with the excitons, scattering with other carriers and with phonons leads to thermalisation of the biexciton population. The rate of radiative recombination of the biexcitons is determined using parameters from [49]. Biexcitons are more localised than single excitons and can self-trap, exerting a deformation potential of  $\mathcal{E}_{DP} = 1.74$  eV to the lattice which can lead to the breaking of a carbon-carbon bond [33].

Mauri *et al.* proposed that following self-trapping, radiative recombination of the biexciton would follow with a large Stokes shift of 3.23 eV on timescales of  $\tau_r \sim 7$  ns leaving a single exciton and the lattice partially distorted, leading to a localised graphitization [33]. Here we propose an alternative mechanism, a non-radiative recombination pathway, transferring the energy of the entire biexciton to the lattice and forming a Frenkel defect.

The energetics of this proposed process are depicted in FIG. 2. The self-trapped biexciton (STbX) localised on the broken bond has a minimum energy of 8.9 eV which makes the formation of a 7.14 eV Frenkel defect energetically favourable. The driving force behind the process is depicted in FIG. 2b. The STbX takes the form of two deep levels within the band-gap, a doubly occupied anti-bonding level 1.7 eV below the conduction band edge and an empty bonding level 1.6 eV above the valence band maximum, both localised on the broken bond [33]. It is therefore possible that further deformation of the lattice pushes the deep levels towards mid-gap as shown in FIG. 2b allowing recombination through electron capture and creating the Frenkel defect.

Similar processes are known to occur in other materials. Bang *et al.* showed that 2 electron-hole pairs within InGaN can non-radiatively recombine via the formation and recombination of a Frenkel pair [55] and self trapped excitonic states have been shown to lead to the permanent formation of Frenkel defects in SiO<sub>2</sub> and other dielectrics [32] [56] [57]. In both cases, the deformation of the lattice leads to the formation of states within the band-gap that allow energy transfer from the electronic system to the lattice.

The typical Frenkel defect formation time is calculated from the STbX population, determined by a thermally activated electron capture process [58].

$$\tau_{FD}(r, z, t, \mathcal{E}) = \frac{h}{\mathcal{E}_{ph}} \times \exp\left(\frac{\mathcal{E}_b - (\mathcal{E} - [2(\mathcal{E}_C - \mathcal{E}_X) - \mathcal{E}_{bX} - \mathcal{E}_{DP}])}{k_B T_L(r, z, t)}\right) \quad (1)$$

where  $\mathcal{E}_{ph}$  is the optical phonon energy,  $\mathcal{E}_b$  is the energy barrier [55],  $\mathcal{E}_C$  is the conduction band minimum and  $T_L$  is the lattice temperature. The value  $\mathcal{E}$  refers in this case to the energy of the self-trapped biexciton and the term within the square brackets is the minimum possible energy of a self-trapped biexciton. The height of the energy barrier is established by assuming that the shape of the self trapped biexciton potential energy surface is symmetric about its minimum and that the formation energy is equal to the activation energy minus a quarter of the relaxation energy of the lattice which holds in the high temperature limit [58]. For the STbX, this suggests an energy barrier of  $1.74 - \frac{4.85}{4} = 0.53$  eV. This value is consistent with our experimental data and is discussed further in section 5. Using this value of  $\mathcal{E}_b$  in equation (1) results in a lifetime for Frenkel defect formation that is shorter than the radiative lifetime of the STbX for lattice temperatures above about 450K.

We neglect any processes that are facilitated by the creation of the Frenkel defects. This is a reasonable assumption since defect formation does not begin until several picoseconds after the optical pulse has passed. We also ignore any recombination of Frenkel defects, although the recombination of a fixed fraction of the defects would ap-

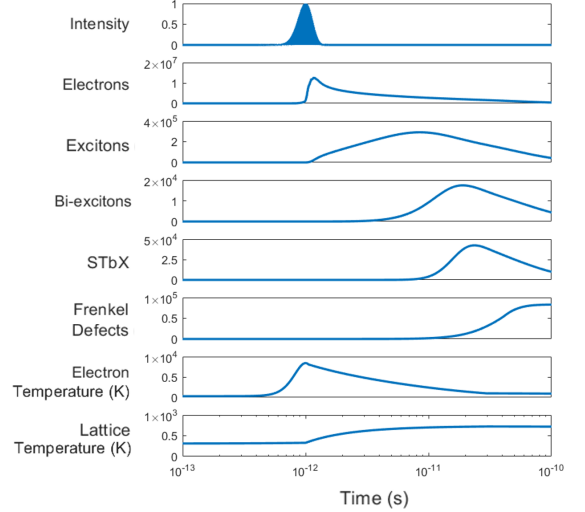


FIG. 3. Time dependence of parameters simulated in the PDE model. The peak of the laser pulse is set to 1 ps to facilitate a logarithmic time scale capturing the range of dynamics. Through charge neutrality, the number of holes is equal to the number of electrons.

pear as a scaling factor and would otherwise not alter the results of the model.

#### IV. GENERAL CHARACTERISTICS

FIG. 3 displays the simulated time dynamics for the various parameters generated by an 6 nJ, 250 fs pulse at the focus of the laser pulse, allowing the relative timings of the processes to be observed. Electron generation occurs quickly during and following the pulse, initially via photoionisation but the majority being generated later via cascade processes. The electron concentration peaks around 0.25 ps after the peak of the pulse intensity and then decays multi-exponentially due to non-radiative recombination processes such as Auger processes and excitonic formation. Rapid carrier-carrier scattering ensures that the different carrier types are at thermal equilibrium with each other and re-ionises the majority of any excitonic states that form. Immediately after the pulse the carrier temperature reaches several thousand degrees while lattice temperature remains low. Electron-phonon scattering then causes the carrier temperature to decay rapidly and the lattice temperature to increase until equilibrium is reached after around 30 ps.

The cooling of the hot carriers also triggers the increase of exciton and then biexciton populations, with peak populations at times of about 9 ps and 20 ps after the laser pulse. The STbX population and the resulting population of Frenkel defects then follow some 22 ps and 30 ps after the laser pulse has passed respectively. We note that by this time the lattice temperature is sufficiently high that the proposed thermally activated Frenkel defect



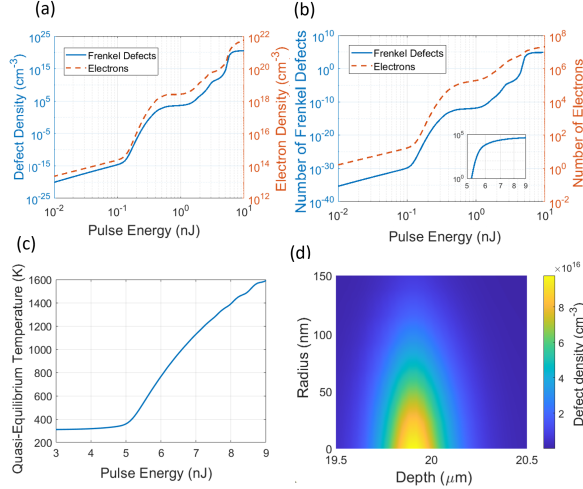


FIG. 4. a. Maximum densities of carriers and defects generated against pulse energy. In red the number of electrons that are created against pulse energy and in blue, the simulated number of defects generated. b. Numerical integration of the coupled PDE model over energy, space and time. Inset displays the number of defects generated with probability above 1. c. The quasi-equilibrium temperature reached by the electron-lattice system at the centre of focus against pulse energy. d. Simulated spatial distribution of defects from a pulse of 5.5 nJ focused 20  $\mu\text{m}$  into the diamond. The laser beam is incident from the left-hand side.

formation process will be considerably faster than radiative recombination of the STbX discussed by Mauri *et al.*. At  $\sim 20$  ps the electron and lattice temperatures reach a quasi-equilibrium. This temperature will then decay over timescales of order microseconds through thermal diffusion.

FIG. 4a and b shows the peak density and total number of photogenerated electrons as a function of write-pulse energy along with the peak density and total number of Frenkel defects generated per pulse. The photoelectron generation curve follows a similar dependency to that from photoionisation alone as shown by Lagomarsino *et al.* [37], (FIG. S3 in the supplementary information), however the impact ionisation increases and smooths out the number of electrons generated. At high pulse energies there is an uptick in the non-linearity of carriers at the centre of focus. This is because carrier densities become high enough that the carrier mobility rapidly decreases leading to an accelerated carrier avalanche. This is rapidly saturated as Auger processes reach a quasi-equilibrium with the impact ionisation and plasma effects suppress photoionisation. Away from the centre of the focus, growth continues to occur leading to a smoothing out of the total number of carriers.

For pulse energies below about 4 nJ the defect generation curves in FIG. 4a and b follow a similar pattern to that of electron generation, but with a non-linearity about four times larger due to the biexciton-induced for-

mation mechanism. The Frenkel defect generation probability passes 1 at  $\sim 5$  nJ with a fast rise in the number of defects generated over a very small range in pulse energies which quickly saturates. This extremely steep dependence of defect formation on pulse energy occurs primarily as a result of two effects. The reduced carrier mobility not only produces an accelerated carrier avalanche but also leads to a significantly accelerated formation of excitonic states following cooling of the carriers. In addition, the temperature at which the electron-lattice system reaches a quasi-equilibrium for these pulse energies becomes significant, this accelerates the non-radiative recombination of the self trapped biexcitons in competition with radiative processes. The quantum efficiency for Frenkel defect formation, defined as  $\eta = \frac{\tau_r}{\tau_r + \tau_{FD}}$  and using equation (1), where  $\tau_r$  is the radiative recombination timescale, rises from  $\sim 10^{-3}$  at room temperature to near unity at temperatures above 500 K. The peak quasi-equilibrium temperature reached by the carrier-lattice system against pulse energy is shown in FIG. 4c. At low pulse energies the maximum carrier densities are low enough that the quasi-equilibrium temperature reached is not significantly above the ambient temperature, however for higher pulse energies, it rises rapidly such that Frenkel defect formation will quickly become efficient over radiative recombination processes.

The rapid saturation in Frenkel defect number in FIG. 4a and b is again attributed to two processes. At these high pulse energies, there is a saturation to the electron density growth which becomes high enough that efficient Auger processes take equal precedence with avalanche ionisation. In addition, the non-radiative recombination of self-trapped biexcitons becomes efficient compared with radiative processes as the electron-lattice equilibrium temperature is high.

The spatial distributions of the generated Frenkel defects at pulse energies of 5.5 nJ and 7 nJ are shown in FIG. 4d and FIG. S5. At the lower pulse energy the distribution approximately follows the diffraction limited focal intensity distribution of the microscope scaled by the non-linearity, while at the higher pulse energy a distortion is observed that results from the metal-like properties of the high density of free carriers [32] [30] [59]. This changes the focusing of the incoming light leading to absorption at shallower depths and attenuation of the beam, altering the spatial distribution of defect formation. The simulated full-width half maximum (FWHM) for the 5.5 nJ pulse is  $\sim 250$  nm in depth and  $\sim 50$  nm in radius. These values are very similar to the measured positional accuracy of laser written NV centers by Chen *et al.* [16]. Whilst this is not a direct comparison since the model does not include the annealing required to form NV centres from the Frenkel defects, the consistency between the two gives further confidence in the simulation results.

## V. COMPARISON WITH EXPERIMENTAL DATA

In the experiments, the onset of visible GR1 fluorescence occurs at a pulse energy of about 16 nJ, almost three times higher than that predicted from the simulation results of FIG. 4. There are a number of possible reasons for this discrepancy, including unaccounted aberrations in the focal spot, an underestimate of optical losses and pulse dispersion between the objective lens and the focal spot, and inaccuracies in parameters such as scattering rates and binding energies that will influence the efficiency of biexciton formation. We treat this unknown scaling factor as a fitting parameter. A second scaling factor is needed in order to compare the number of Frenkel defects generated with the measured GR1 fluorescence intensity. This scaling factor is dependent on the fluorescence quantum efficiency of the GR1 defects and on the efficiency of the fluorescence microscope used for the measurements. Respective values of 2.84 and 3.47 were found for these two scaling factors, providing the fit shown in FIG. 1 with an  $R^2$  of 0.9977 and adjusted  $R^2$  of 0.9976. These scaling factors were found by first taking the base 10 logarithm of the model and experimental data such that linear regression could be used. Transmission of light through the objective lens accounts for  $\sim 30\%$  of the loss such that the  $x$  scaling due to small deviations in the perceived focus from the true focus and from other losses can be given as approximately a factor of 2. The magnitude of deviations from the true focus likely account for most of this through imperfect aberration correction.

FIG. 5a and b reveal the sensitivity of the model to the energy barrier height  $\mathcal{E}_b$ . Each simulation curve is scaled on both the  $x$  and  $y$  axes as described above to provide a best fit to the experimental data. FIG. 5a reveals that the magnitude of the energy barrier plays a significant role in determining the magnitude of the non-linearity. The sum of the squared residual distance between the experimental data and the model is plotted versus  $\mathcal{E}_b$  in FIG. 5b. A polynomial fit reveals that the residuals are minimised at a value of  $\mathcal{E}_b = 0.47 \pm 0.01$  eV with a direct overlay shown on-top of the experimental data shown in FIG. 1c. The high degree of agreement between the model and experiment gives weight to the hypothesis that most of the energy required to form a Frenkel defect comes from the recombination of self-trapped biexcitonic states. In addition, the need for biexcitonic states explain the localisation of energy to single lattice sites.

Finally we explore the dependence of Frenkel defect generation on two practical parameters: the numerical aperture (NA) of fabrication laser focus and the duration of the laser pulse. Reducing the NA of the focusing lens reduces the focal intensity and thereby increases the pulse energy needed for defect generation. In addition some modest change in the dynamics might be expected as a result of a reduction in carrier diffusion. We set initial conditions for various focusing NA, ranging between

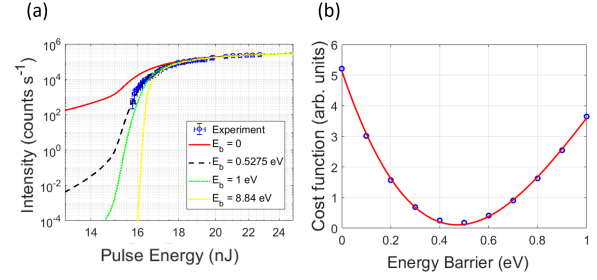


FIG. 5. a. Simulated defect vs pulse energy curves for different values of  $\mathcal{E}_b$  fitted to experimental data through non-linear least squares fitting. b. Minimisation of the cost function for the energy barrier to non-radiative recombination reveals a value of  $\mathcal{E}_b = 0.47 \pm 0.01$  eV fits best to the experimental data.

NA of 0.95 and 1.4. The corresponding simulated and experimental data are seen in FIG. 6a.

Here, pulse energies are seen that are well above those which graphitised the material in the earlier experiments, however the threshold for graphitisation increases alongside the threshold for defect generation due to the reduced peak focal intensities observed from the differing initial conditions. As before, the shapes of the data-sets and relative distances between them are the important parameters when comparing to experiment rather than the absolute values of pulse energies due to the assumptions of perfect aberration correction and no losses of light during focusing. One should note that these data-sets were taken following a realignment of the optical path from the laser to the sample and hence have a lower threshold pulse energy for generation. This also means that the scaling parameter for the  $x$  axis for comparison of the simulation and experiment is reduced from that in previous figures.

The general trend described above is visible in both the simulation results and experimental data. We note that in the experiments, a numerical aperture of 1.4 showed no reduction in required pulse energy compared with NA = 1.25. This could indicate the presence of uncorrected aberrations such that the outermost rays passing through the objective do not contribute measurably to the peak focal intensity. Also the required increase in pulse energy for NA = 0.95 is somewhat larger than predicted. FIG. 6b shows the same experimental data with the simulation data-sets independently scaled to provide best fits. The dependence on relative pulse energy does not vary substantially with NA and the simulations fit well to the data throughout.

The effect of varying the pulse duration between 120 fs and 1 ps is shown in FIG. 6c and d where, as above, panel d includes a re-scaling of the individual simulation data-sets to provide best fits to the experimental data. A particularly marked effect that needs to be taken into effect when simulating different pulse durations is dispersion of the pulse as it passes through the focusing optics and the material. This is hard to quantify and

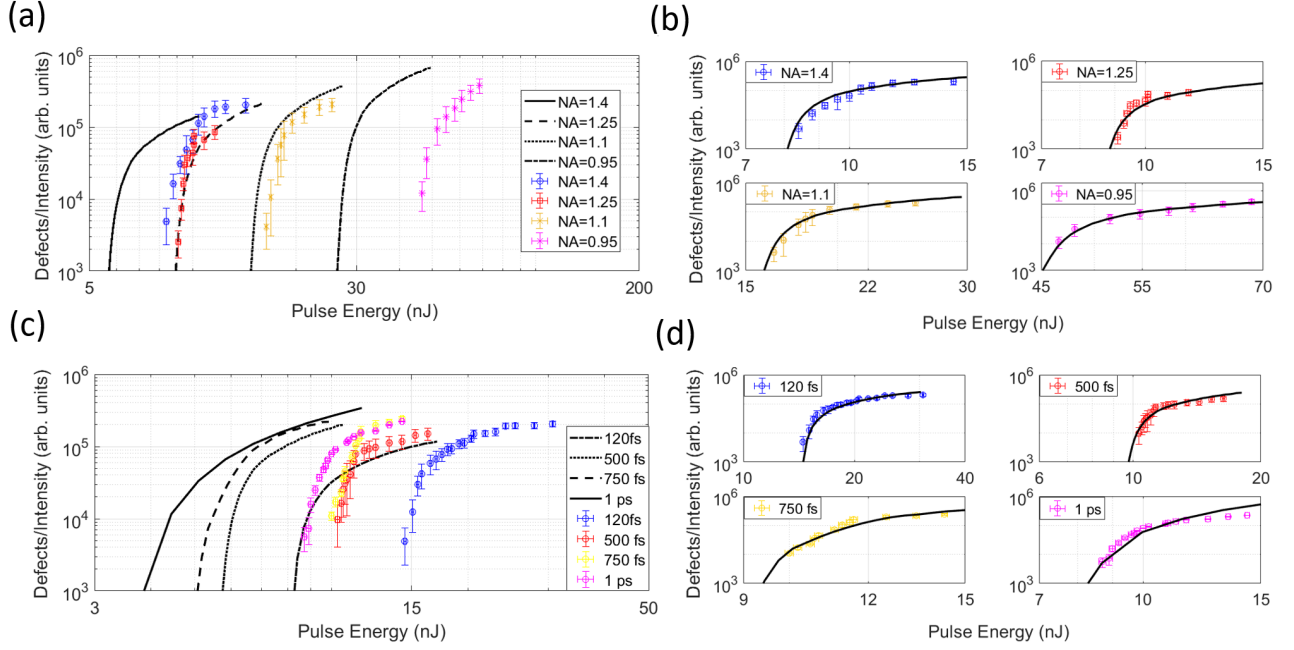


FIG. 6. a. Simulated (lines) defect generation probability as a function of pulse energy for differing NA of focus under the assumption of no optical losses alongside experimental data (points). The NA's range from 0.95 to 1.4. b. Data and simulation for differing NA of focus overlaid to show agreement in the non-linearity through multiplication of simulated data by constants in x and y. c. Simulated (lines) defect generation probability as a function of pulse energy for differing pulse durations under the assumption of no optical losses alongside experimental data (points). The pulse durations range from 120 fs to 1 ps. d. Data and simulation for differing pulse durations overlaid to compare the non-linearity through multiplication of simulated data by constants in x and y.

is highly dependent upon the specific lens used. Literature values of group delay dispersion (GDD) for numerical apertures of 1.4 for ultra-short pulses range between 4000-8000 fs<sup>2</sup> [66][67]. This will lead to broadening of 120 fs pulses to the range 150 - 220 fs but pulses of 500 fs or greater will be negligibly broadened. The effect of this is to shift the 120 fs pulse curve towards those of the longer pulses. A value of GDD = 6000 fs<sup>2</sup> was chosen for the simulations which causes the 120 fs pulse to broaden to 185 fs whereas the 500 fs pulse broadens to 501 fs. Somewhat counter-intuitively, the general trend in both experimental data and the simulation results is for shorter pulses to require higher pulse energies for defect generation. This is because, although shorter pulses achieve the same focal intensity for lower pulse energy, they generate fewer carriers due to a reduction in free carrier absorption and subsequent impact ionisation [15]. An x-axis scaling parameter of approximately two allows conversion between each simulation and its experimental counterpart, the cause of which is likely due to imperfect aberration control. Experimentally, the observed non-linearity is again relatively unchanged; in contrast the model predicts a noticeable reduction in non-linearity for the longest pulses.

## VI. CONCLUSION

In summary, we have studied the generation of Frenkel defects in diamond in response to a single, sub-picosecond laser pulse. Experimental data show a strong non-linearity at the onset of Frenkel defect generation, followed by rapid saturation in the number of Frenkel defects created. A finite-difference time-domain model based on coupled non-linear rate equations describes the carrier excitation and relaxation processes, with Frenkel defect formation attributed to the thermally activated non-radiative relaxation of self-trapped biexcitons. The model shows good agreement with experimental data for the dependence of defect formation on pulse energy, and an activation barrier height of  $470 \pm 10$  meV is derived from fit. The effects of laser focal spot size and pulse duration were explored, revealing that impact ionisation of hot carriers is an important contributing factor in generating the high carrier densities needed, such that longer pulses, in which carrier heating plays a more significant role, generate defects more efficiently than do shorter pulses.

The model described here will assist in the optimisation of fabrication parameters for the defect engineering of materials in solid-state quantum devices and lead towards greater understanding of ultra-fast laser interac-



tion with wide-bandgap materials. Future work could generalise this model to other materials as many of the processes described, such as photoionisation, are readily adaptable for other materials given different empirical parameters and band-structure, or the model could be adapted to describe laser annealing processes as reported in [16].

## VII. ACKNOWLEDGMENTS

This work is supported by the UK Hub in Quantum Computing and Simulation, part of the UK National Quantum Technologies Programme with funding from UKRI EPSRC grant EP/T001062/1 and additional

support was received from EPSRC grant (Grant No. EP/R004803/01).

The coupled differential equation model was developed and numerically solved by Benjamin Griffiths. Discussions with Jason Smith, Patrick Salter, Martin Booth, Shannon Nicley, Joanna Zajac and Gavin Morley enabled clarification on various mechanisms. The band-structure was calculated by Andrew Kirkpatrick. Direct laser writing was performed by Benjamin Griffiths and Patrick Salter and fluorescence characterisation was conducted by Benjamin Griffiths, Rajesh Patel and Shannon Nicley. Data analysis and fitting of the model to experiment was conducted by Benjamin Griffiths. The manuscript was written by Benjamin Griffiths and Jason Smith in discussions with Patrick Salter and Joanna Zajac.

- 
- [1] X. Rong, J. Geng, F. Shi, Y. Liu, K. Xu, W. Ma, F. Kong, Z. Jiang, Y. Wu, J. Du, Experimental fault-tolerant universal quantum gates with solid-state spins under ambient conditions, *Nat Commun.* 6, 8748 (2015).
  - [2] C. Simon, M. Afzelius, J. Appel, A. Boyer de la Giroday, S. J. Dewhurst, N. Gisin, C. Y. Hu, F. Jelezko, S. Krll, J. H. Miller, J. Nunn, E. S. Polzik, J. G. Rarity, H. De Riedmatten, W. Rosenfeld, A. J. Shields, N. Skld, R. M. Stevenson, R. Thew, I. A. Walmsley, M. C. Weber, H. Weinfurter, J. Wrachtrup, R. J. Young, *Quantum Memories*, *Eur. Phys. J. D.* 58, 122 (2010).
  - [3] F. Jelezko, T. Gaebel, I. Popa, M. Domhan, A. Gruber, J. Wrachtrup, Observation of Coherent Oscillation of a Single Nuclear Spin and Realization of a Two-Qubit Conditional Quantum Gate, *Phys. Rev. Lett.* 93, 130501 (2004).
  - [4] G. Balasubramanian, P. Neumann, D. Twitchen, M. Markham, R. Kolesov, N. Mizuochi, J. Isoya, J. Achard, J. Beck, J. Tessler, V. Jacques, P. R. Hemmer, F. Jelezko, J. Wrachtrup, Ultralong spin coherence time in isotropically engineered diamond, *Nat. Mater.* 8 5, 383-387 (2009).
  - [5] M. V. Gurudev Dutt, L. Childress, L. Jiang, E. Togan, J. Maze, F. Jelezko, A. S. Zibrov, P. R. Hemmer, M. D. Lukin, Quantum Register Based on Individual Electronic and Nuclear Spin Qubits in Diamond, *Science*, 316, 1312 (2007).
  - [6] S. Pezzagna, J. Meijer, Quantum computer based on color centers in diamond, *Appl. Phys. Rev.* 8, 011308 (2021).
  - [7] A. G. Alekseev, V. N. Amosov, A. V. Krasilnikov, S. N. Tugarinov, V. V. Frunze, and A. Yu Tsutsikh. Transformation of GRI defects in annealed natural type IIa diamonds. *Tech. Phys. Lett.* 26, 496498 (2000).
  - [8] I. Kiflawi, A. T. Collins, K. Iakoubovskii and D. Fisher, Electron irradiation and the formation of vacancy-interstitial pairs in diamond, *J. Phys. Condens. Matter.* 19, 046216 (2007).
  - [9] Y. C. Chen, P. Salter, S. Knauer, L. Weng, A. C. Frangeskou, C. J. Stephen, S. N. Ishmael, P. R. Dolan, S. Johnson, B. L. Green, G. W. Morley, M. E. Newton, J. G. Rarity, M. J. Booth, J. M. Smith, Laser writing of coherent color centres in diamond, *Nature Photon.* 11, 7780 (2017).
  - [10] B. Sotillo, V. Bharadwaj, J. P. Hadden, S. Rampini, A. Chiappini, T. T. Fernandez, C. Armellini, A. Serpengzel, M. Ferrari, P. E. Barclay, R. Ramponi, S. M. Eaton, Visible to Infrared Diamond Photonics Enabled by Focused Femtosecond Laser Pulses, *Micromachines.* 8, 60, (2017).
  - [11] C. J. Stephen, B. L. Green, Y. N. D. Lekhai, L. Weng, P. Hill, S. Johnson, A. C. Frangeskou, P. L. Diggle, Y.-C. Chen, M. J. Strain, E. Gu, M. E. Newton, J. M. Smith, P. S. Salter, G. W. Morley, Deep Three-Dimensional Solid-State Qubit Arrays with Long-Lived Spin Coherence, *Phys. Rev. Applied.* 12, 064005 (2019).
  - [12] V. Yurgens, J. A. Zuber, S. Flagan, M. De Luca, B. J. Shields, I. Zardo, P. Maletinsky, R. J. Warburton, and T. Jakubczyk, Low charge-noise nitrogen-vacancy centres in diamond created using laser writing with a solid-immersion lens, *ACS Photonics*, 8, 6, 17261734 (2021).
  - [13] Y. C. Chen, P. S. Salter, M. Niethammer, M. Widmann, F. Kaiser, R. Nagy, N. Morioka, C. Babin, J. Erlekampf, P. Berwian, M. J. Booth, J. Wrachtrup, Laser Writing of Scalable Single Color centres in Silicon Carbide, *Nano Lett.* 19, 4, 23772383 (2019).
  - [14] S. Castelletto, J. Maksimovic, T. Katkus, T. Ohshima, B. C. Johnson, S. Juodkazis, Color centres Enabled by Direct Femto-Second Laser Writing in Wide Bandgap Semiconductors, *Nanomaterials.* 11, 1, 72 (2021).
  - [15] T. Kurita, N. Mineyuki, Y. Shimotsuma, M. Fujiwara, N. Mizuochi, M. Shimizu, K. Miura, Efficient generation of nitrogen-vacancy center inside diamond with shortening of laser pulse duration, *Appl. Phys. Lett.* 113, 211102 (2018).
  - [16] Y. C. Chen, B. Griffiths, L. Weng, S. S. Nicley, S. N. Ishmael, Y. Lekhai, S. Johnson, C. J. Stephen, B. L. Green, G. W. Morley, M. E. Newton, M. J. Booth, P. S. Salter, J. M. Smith, Laser writing of individual nitrogen-vacancy defects in diamond with near-unity yield, *Optica* 6, 662-667 (2019).
  - [17] T. Kurita, Y. Shimotsuma, M. Fujiwara, M. Fujie, N. Mizuochi, M. Shimizu, K. Miura, Direct writing of high-density nitrogen-vacancy centers inside diamond by femtosecond laser irradiation, *Appl. Phys. Lett.* 118, 214001 (2021).
  - [18] R. D. Simmonds, P. S. Salter, A. Jesacher, M. J. Booth,

- Three dimensional laser microfabrication in diamond using a dual adaptive optics system, *Opt. Express*. 19, 2412224128 (2011).
- [19] T. V. Kononenko, M. Meier, M. S. Komlenok, S. M. Pimenov, V. Romano, V. P. Pashinin, V. I. Konov, Microstructuring of diamond bulk by IR femtosecond laser pulses, *Appl. Phys. A*. 90, 645651 (2008).
  - [20] J. P. Hadden, V. Bharadwaj, B. Sotillo, S. Rampini, R. Osellame, J. D. Witmer, H. Jayakumar, T. T. Fernandez, A. Chiappini, C. Armellini, M. Ferrari, R. Ramponi, P. E. Barclay, S. M. Eaton, Integrated waveguides and deterministically positioned nitrogen vacancy centres in diamond created by femtosecond laser writing, *Opt. Lett.* 43, 3586-3589 (2018).
  - [21] N. Medvedev, H. O. Jeschke, B. Ziaja, Nonthermal phase transitions in semiconductors induced by a femtosecond extreme ultraviolet laser pulse, *New J. Phys.* 15, 015016, (2013).
  - [22] H. O. Jeschke, M. E. Garcia, K. H. Bennemann, Microscopic analysis of the laser-induced femtosecond graphitization of diamond, *Phys. Rev. B* 60, R3701 (1999)
  - [23] C. Z. Wang, K. M. Ho, M. D. Shirk, P. A. Molian, Laser-Induced Graphitization on a Diamond (111) Surface, *Phys. Rev. Lett.* 85, 4092 (2000).
  - [24] V. V. Kononenko, I. I. Vlasov, V. M. Gololobov, T. V. Kononenko, T. A. Semenov, A. A. Khomich, V. A. Shershulin, V. S. Krivobok, V. I. Konov, Nitrogen-vacancy defects in diamond produced by femtosecond laser nanoablation technique, *Appl. Phys. Lett.* 111, 081101 (2017).
  - [25] L. V. Keldysh. Ionization in the field of a strong electromagnetic wave. *Sov. Phys. JETP*. 20, 5, 13071314 (1965).
  - [26] P. K. Kennedy, A First-Order Model for Computation of Laser-Induced Breakdown Thresholds in Ocular and Aqueous Media: Part I-Theory, *IEEE Journal of Quantum Electron.* 31, 12, 2241 (1995).
  - [27] T. Apostolova, Y. Hahn, Modeling of laser-induced breakdown in dielectrics with subpicosecond pulses, *Journal of Applied Physics* 88, 1024 (2000).
  - [28] R. Gattass, E. Mazur, Femtosecond laser micromachining in transparent materials, *Nature Photon.* 2, 219225 (2008).
  - [29] L. V. Keldysh, The electron-hole liquid in semiconductors, *Contemporary Physics*, 27, 5, 395-428 (1986).
  - [30] A. Kaiser, B. Rethfeld, M. Vicanek, G. Simon, Microscopic processes in dielectrics under irradiation by subpicosecond laser pulses, *Phys. Rev. B*. 61, 11437 (2000).
  - [31] K. Plamann, F. Aptel, C. L. Arnold, A. Courjaud, C. Crotti, F. Deloison, F. Druon, P. Georges, M. Hanna, J.-M. Legeais, Ultrashort pulse laser surgery of the cornea and the sclera, *J. Opt.* 12 084002 (2010).
  - [32] S. S. Mao, F. Quere, S. Guizard, X. Mao, R. E. Russo, G. Petite, P. Martin. Dynamics of femtosecond laser interactions with dielectrics. *Applied Physics A*. 79, 7, 16951709 (2004).
  - [33] F. Mauri, R. Carr, First-Principles Study of Excitonic Self-Trapping in Diamond, *Phys. Rev. Lett.* 75, 3166 (1995).
  - [34] P. Deak, B. Aradi, M. Kaviani, T. Frauenheim, A. Gali, Formation of NV centres in diamond: A theoretical study based on calculated transitions and migration of nitrogen and vacancy related defects, *Phys. Rev. B*. 89, 075203 (2014).
  - [35] S. Salustro, Y. Nel, C. M. Zicovich-Wilson, P. Olivero, R. Dovesi, The V + I defects in diamond: An ab initio investigation of the electronic structure, of the Raman and IR spectra, and of their possible recombination, *J. Chem. Phys.* 145, 184701 (2016).
  - [36] M. Barbiero, S. Castelletto, M. Gu, Multi-focal laser fabrication of nitrogen vacancy centres in a bulk diamond, *OSA Continuum* 3, 3416-3423 (2020).
  - [37] S. Lagomarsino, S. Sciortino, B. Obreshkov, T. Apostolova, C. Corsi, M. Bellini, E. Berdermann, C. J. Schmidt, Photoionisation of monocrystalline CVD diamond irradiated with ultrashort intense laser pulse, *Phys. Rev. B*. 93, 085128 (2016).
  - [38] A. Guenther, *Laser induced damage in optical materials*, CRC Press, ISBN 9781138199569 (2019).
  - [39] C. D. Clark, J. Walker, The Neutral Vacancy in Diamond, *Proceedings of the Royal Society A*. 334, 159 (1973).
  - [40] K. W. Böer, U. W. Puhl, *Semiconductor Physics*. Springer, Cham. ISBN 978-3-319-69148-0 (2018).
  - [41] M. Kolesik, J. V. Moloney, Nonlinear optical pulse propagation simulation: From Maxwells to unidirectional equations, *Phys. Rev. E*. 70, 036604, (2004).
  - [42] E. Hecht, *Optics*, Addison-Wesley, ISBN 9780133977226 (2001).
  - [43] A. Jesacher, M. J. Booth, Parallel direct laser writing in three dimensions with spatially dependent aberration correction, *Opt. Express*. 18, 21090-21099 (2010).
  - [44] M. Kozak, F. Trojanek, P. Maly, Optical study of carrier diffusion and recombination in CVD diamond, *Phys. Status Solidi A*. 210, 10 (2013).
  - [45] N. Tandon, J. D. Albrecht, L. R. Ram-Mohan, Electron-phonon coupling and associated scattering rates in diamond, *Diamond and Related Materials*. 56, 1-5 (2015).
  - [46] B. Monserrat, R. J. Needs, Comparing electron-phonon coupling strength in diamond, silicon, and silicon carbide: First-principles study, *Phys. Rev. B*. 89, 214304 (2014).
  - [47] E. I. Lipatov, D. E. Genin, D. V. Grigor'ev, V. F. Tarasenko *Luminescence - An Outlook on the Phenomena and their Applications*, Chapter 9: Recombination Radiation in the diamond, ISBN 978-953-51-2763-5 (2016).
  - [48] H. Morimoto Y. Hazamaa, K Tanaka, N. Naka, Exciton lifetime and diffusion length in high-purity chemical-vapor-deposition diamond, *Diamond and Related Materials*, 63, 47-50 (2016).
  - [49] J. Omachi, T. Suzuki, K. Kato, N. Naka, K. Yoshioka, M. Kuwata-Gonokami, Observation of Excitonic N-Body Bound States: Polyexcitons in Diamond, *Phys. Rev. Lett.* 111, 026402 (2013).
  - [50] C. D. Clark, P. J. Dean and P. V. Harris, Intrinsic edge absorption in diamond, *Proc. R. Soc. London, Ser. A*. 277, 312. (1964).
  - [51] H. Katow, J. Usukura, R. Akashi, K. Varga, S. Tsuneyuki, Numerical investigation of triexciton stabilization in diamond with multiple valleys and bands, *Phys. Rev. B*, 95, 125205 (2017).
  - [52] S. M. Bennington, R. I. Bewley, T. E. Weller, Using tip enhanced femtosecond lasers to create graphite nanostructures on diamond, STFC Central Laser facility, Annual Report 2008/2009, 204 (2008).
  - [53] P. Stampfli, K. H. Bennemann, Theory for the instability of the diamond structure of Si, Ge, and C induced by a dense electron-hole plasma, *Phys. Rev. B*. 42, 7163 (1990).
  - [54] P. E. Selbmann, In: Hess K. *Hot Carriers in Semicon-*

- ductors. Springer, Boston, MA. ISBN 978-1-4613-0401-2 19-22 (1996).
- [55] J. Bang, Y. Y. Sun, J-H. Song, S. B. Zhang, Carrier-induced transient defect mechanism for non-radiative recombination in InGaN light-emitting devices, *Scientific Reports*. 6, 24404 (2016).
  - [56] N. Itoh, T. Shimizu-Iwayama, T. Fujita. Excitons in crystalline and amorphous SiO<sub>2</sub>: formation, relaxation and conversion to Frenkel pairs. *J. Non. Cryst. Solids*. 179, 194201 (1994).
  - [57] T. T. Williams, K. S. Song, W. L. Faust, C. H. Leung, Off-centre self-trapped excitons and creation of lattice defects in alkali halide crystals. *Phys. Rev. B*. 33, 7232 (1986).
  - [58] A. Shenk, A model for the field and temperature dependence of Shockley-Read-Hall lifetimes in silicon. *Solid-State Electronics* 35, 11, 1585-1596 (1992).
  - [59] M. Combescot, J. Bok, Electron-hole plasma generation and evolution in semiconductors, *Journal of Luminescence*, 30, 14, 1-17 (1985).
  - [60] Goodman, J. W. Introduction to Fourier optics. New York: McGraw-Hill, ISBN 0-07-024254-2 (1996).
  - [61] V. E. Gruzdev, Photoionization rate in wide band-gap crystals, *Phys. Rev. B*. 75, 205106 (2007).
  - [62] S. J. Clarke, M. Segall, C. J. Pickard, P. J. Hasnip, M. Probert, K. Refson, M. C. Payne *Z Kristallogr Cryst Mater*. 220, 5-6, 567-570 (2004).
  - [63] P. Perdew, M. Ernzerhof, *J. Chem. Phys.* 105, 22, 9982-9985 (1996).
  - [64] S. V. Popruzhenko, Keldysh theory of strong field ionization: history, applications, difficulties and perspectives, *J. Phys. B: At. Mol. Opt. Phys.* 47, 204001 (2014).
  - [65] Y. R. Shen, *The Principles of Nonlinear Optics*. New York: Wiley, ISBN 978-0-471-43080-3 (1984).
  - [66] J. B. Guild, C. Xu, W. W. Webb, Measurement of group delay dispersion of high numerical aperture objective lenses using two-photon excited fluorescence, *Applied Optics*. 36, 1, 397-401 (1997).
  - [67] P. Xi, Y. Andegeko, D. Pestov, V. V. Lozovoy, M. M. Dantus, Two-photon imaging using adaptive phase compensated ultrashort laser pulses, *J. of Biomedical Optics*, 14, 1, 014002 (2009).
  - [68] See Supplemental Material at [URL will be inserted by publisher] for an outline of the optical apparatus used for laser writing and the coupled partial differential equation model used in this work.